Biochemistry and Biophysics Reports 27 (2021) 101039

Contents lists available at ScienceDirect

Biochemistry and Biophysics Reports

journal homepage: www.elsevier.com/locate/bbrep

# Helical reconstruction of *Salmonella* and *Shigella* needle filaments attached to type 3 basal bodies

Vadim Kotov [a,b,c,1,2], Michele Lunelli [a,d,1], Jiri Wald [a,b,c], Michael Kolbe [a,d,e,*], Thomas C. Marlovits [a,b,c,**]

[a] Centre for Structural Systems Biology (CSSB), Notkestraße 85, 22607 Hamburg, Germany
[b] University Medical Centre Hamburg-Eppendorf (UKE), Martinistraße 52, 20246 Hamburg, Germany
[c] Deutsches Elektronen-Synchrotron (DESY), Notkestraße 85, 22607 Hamburg, Germany
[d] Department of Structural Infection Biology, Helmholtz Centre for Infection Research (HZI), Inhoffenstraße 7, 38124 Braunschweig, Germany
[e] Department of Chemistry, Faculty of Mathematics, Informatics and Natural Sciences, University of Hamburg, Rothenbaumchaussee 19, 20148 Hamburg, Germany

ARTICLE INFO

*Keywords:*
Type 3 secretion system
Cryo electron microscopy
Needle filament
Helical reconstruction
*Shigella*
*Salmonella,* host-pathogen interaction

ABSTRACT

Gram-negative pathogens evolved a syringe-like nanomachine, termed type 3 secretion system, to deliver protein effectors into the cytoplasm of host cells. An essential component of this system is a long helical needle filament that protrudes from the bacterial surface and connects the cytoplasms of the bacterium and the eukaryotic cell. Previous structural research was predominantly focused on reconstituted type 3 needle filaments, which lacked the biological context. In this work we introduce a facile procedure to obtain high-resolution cryo-EM structure of needle filaments attached to the basal body of type 3 secretion systems. We validate our approach by solving the structure of *Salmonella* PrgI filament and demonstrate its utility by obtaining the first high-resolution cryo-EM reconstruction of Shigella MxiH filament. Our work paves the way to systematic structural characterization of attached type 3 needle filaments in the context of mutagenesis studies, protein structural evolution and drug development.

## 1. Introduction

Pathogenic type 3 secretion systems are specialized infection machinery used by Gram-negative pathogens such as *Salmonella, Shigella, Pseudomonas* and *Yersinia* to invade their eukaryotic hosts [1]. The central component of a type 3 secretion system is a syringe-like protein complex termed the needle complex or the injectisome. The injectisome consists of ring structures embedded in the inner and outer membrane of the bacterium (basal body), a dynamic cytoplasmic complex (sorting platform), a needle filament that begins inside the periplasmic segment of the basal body and protrudes into the environment, and a highly conserved complex which connects the sorting platform and needle (export apparatus). The needle filament is capped with the tip structure that forms pores in the host membrane [2,3]. The effector proteins are unfolded at the interface between the sorting platform and the export apparatus and translocated via the hollow needle filament in an ATP and proton-motive force dependent manner. Upon refolding in the host cytoplasm, the effector proteins manipulate the cellular metabolism to promote the bacterial infection [1].

The needle filament presents an attractive drug target, because it is essential for type 3 mediated infection and is exposed to the extracellular space. Structural studies of the needle filament, however, were hindered by its polymeric nature, which prevented crystallization or solution-state NMR analysis. The first high-resolution insights of the protomer structure were gained from NMR analysis and crystallization of mutants with impaired polymerization [4,5]. These results were complemented by negative-staining and cryo-electron microscopy (cryo-EM) of polymerized needle filaments [6], which revealed the overall architecture and the helical parameters of the needle filament. The comprehensive model of the needle filament structure for *Salmonella* PrgI was first obtained in 2012 by a combination of solid-state NMR and Rosetta modeling [7]. For *Shigella* MxiH this approach was further improved to

* Corresponding author. Centre for Structural Systems Biology (CSSB), Notkestraße 85, 22607 Hamburg, Germany.
** Corresponding author. Centre for Structural Systems Biology (CSSB), Notkestraße 85, 22607 Hamburg, Germany.
*E-mail addresses:* Michael.Kolbe@helmholtz-hzi.de (M. Kolbe), thomas.marlovits@cssb-hamburg.de (T.C. Marlovits).
[1] - equal contribution.
[2] present address: European Molecular Biology Laboratory (EMBL), Hamburg Unit, Notkestraße 85, 22607 Hamburg, Germany.

https://doi.org/10.1016/j.bbrep.2021.101039
Received 12 January 2021; Accepted 26 May 2021
Available online 27 June 2021

integrate a 7 Å cryo-EM structure [8]. Finally, high-resolution cryo-EM structures of *Salmonella* PrgI needle filaments were published recently [9,10].

With the exception of the work by Guo and co-authors [9] all known structures of type 3 needle filaments were solved from isolated filaments in the absence of the basal body, which raises the concern that they do not represent a biologically relevant conformation. Guo et al. demonstrated that cryo-EM maps of *Salmonella* PrgI needle filament obtained from either reconstituted *in vitro* or attached to the basal body are essentially the same to the accuracy of the reconstruction (3.7 Å gold-standard resolution). On the other hand, the authors demonstrated that subtle changes in the PrgI structure induced by point mutations may lead to dramatic differences in functionality. Thus, it cannot be excluded that the attached state of the needle filament contains subtle but functionally relevant differences from the detached state. Ultimately, this issue calls for more needle filament structures obtained from different species and mutants.

Selection of filaments for helical reconstruction is commonly done by manual picking, a tedious and time-consuming process. Algorithms for automatic picking of helical structures were also introduced [11–14], however, their performance might be impaired when the helical structures are attached to bulky particles, such as type 3 basal bodies. In this work we establish a simple procedure to obtain the coordinates of straight filaments attached to another structure, preserving their polarity, and perform helical reconstruction. We validate our approach with the *Salmonella* type 3 needle filament (PrgI) attached to the basal body and subsequently apply it to obtain the highest resolution to date for *Shigella* needle filament (MxiH). We discuss the differences observed in the structure of the attached MxiH needle filament compared to the model determined previously from solid-state NMR and cryo-EM [8] and their functional implications.

## 2. Materials and methods

### 2.1. Needle complex purification and cryo-EM data acquisition

*Salmonella* type 3 needle complexes from *Salmonella* pathogenicity island 1 (SPI-1) were purified from strain *SB905* according to published protocols [15], data collection using graphene-oxide grids was performed as described previously [16]. *Shigella* type 3 needle complex purification and cryo-EM data acquisition was described previously [17].

### 2.2. Helical reconstruction

Helical segments of type 3 needle filaments attached to the basal body were extracted as described in the main text with box size of 300 pixels. All subsequent reconstruction steps were performed in Relion version 3 [11,18]. The dataset was cleaned up using 2D classification (clustering in machine-learning terms), segments with apparent high-resolution features were subjected to a round of 3D refinement. A soft-edged cylinder with 95 Å diameter served as the initial model. Initial values for helical parameters were set from NMR structures [7,8] with search range ± 10%. The first 3D refinement was sufficient to reach ~7 Å gold-standard resolution, and the output map was subjected to one or more rounds of 3D refinement to reach below 4 Å gold-standard resolution after standard post-processing using a soft mask built from the central 30% of the helical reconstruction. Subsequently, CTF refinement and particle polishing procedures followed by additional 3D refinements were used to obtain the final maps (Table 1). Before modeling the maps were locally filtered (Relion procedure), B-factor sharpened and symmetrized using refined helical parameters, based on the pixel values within a central Z length of 30% the box size.

**Table 1**
Cryo-EM data collection, refinement and validation statistics.

| | *Salmonella* | *Shigella* |
|---|---|---|
| **Map** | | |
| EMDB accession code | EMD-11311 | EMD-11312 |
| Pixel size, Å | 1.09 | 1.38 |
| Refined helical rise, Å | 4.4 | 4.3 |
| Refined helical twist, ° | 63.35 | 64.05 |
| Initial segment no. | 308303 | 101369 |
| Final segment no. | 34174 | 19348 |
| Gold-standard resolution, Å | 3.6 | 3.6 |
| **Model** | | |
| PDB accession code | 6ZNH | 6ZNI |
| Non-hydrogen atoms | 14191 | 14812 |
| Number of residues | 1817 | 1886 |
| RMS bond lengths, Å | 0.01 | 0.01 |
| RMS bond angles, ° | 0.83 | 0.61 |
| MolProbity score | 1.67 | 1.77 |
| Clashscore (all-atom) | 4.03 | 6.06 |
| Poor rotamers, % | 3.03 | 2.7 |
| Ramachandran favoured, % | 97.4 | 97.5 |
| Ramachandran allowed, % | 2.6 | 2.5 |
| Ramachandran disallowed, % | 0 | 0 |

### 2.3. Autopicking of helical segments

Relion helical autopicking procedure [11] was used to compare the quality of obtained helical segments with the dataset yielded by the coordinate shift procedure described in the main text. Four high-quality 2D class averages obtained from the coordinate shift procedure were used as references. The sensitivity threshold, minimum average noise and minimum filament length were optimized on five representative micrographs and were set to 0.35, −0.5 and 100 Å for final autopicking on all micrographs. The initial dataset of ~2 million segments was subjected to three rounds of 2D classifications.

### 2.4. Model building

The initial structural model of the PrgI filament was obtained from the solid-state NMR structure [7] (PDB code 2LPZ, model 1), while for MxiH the hybrid structure [8] (PDB code 2MME, model 1).The structures have been fitted into the respective maps with UCSF Chimera 1.14 [19]. The PrgI filament was initially subjected to automatic modeling using StarMap (manuscript in preparation), a Rosetta plugin for UCSF ChimeraX [20]. Both filaments have been manually modeled in the maps with Coot 0.8.9.2 [21] and refined with phenix.real_space_refine 1.17–3644 [22], using the global minimization strategy for the spatial coordinates and the residue-grouped B-factor refinement. Symmetry constraints between subunits and secondary structure restraints were applied. The first methionine residue is not resolved in the protomers. For MxiH also the N-terminal Strep-tag II and factor Xa cleavage site, introduced to isolate the needle complex [17], are not observed in the map. Thus, the PrgI and MxiH subunits include 79 (A2-R80) and 82 (S2-R83) residues, respectively. In total 23 protomers were modeled in each filament, corresponding to more than four turns of the helix. Consequently, at least one subunit is fully interfaced with the neighboring ones.

### 2.5. Normal mode analysis

Normal mode analysis of possible fluctuations in individual protomers and full filaments was performed with R package bio3D version 2.3–4 [23,24] using anisotropic network model on Cα atoms. Per-residue fluctuation values were saved as B-factors in the output PDB files. An R script to run the a full analysis pipeline is available in the Supplemental data 2.

### 2.6. Other software

Scripts to produce helical start-end coordinate files were written in Python3 using modules pandas [25], numpy [26] and gemmi (CCP4, Global Phasing Ltd, https://github.com/project-gemmi/gemmi). Molecular graphics images were produced using the UCSF Chimera [19]. Structures were superposed with the UCSF Chimera MatchMaker tool [27] with default parameters and without including the secondary structure score, but iterating the alignments excluding residue pairs further than 2 Å. Root mean squared deviations (RMSD) were calculated with the Match-Align tool of Chimera. Subunit interface analysis was performed with the PDBePISA server [28]. Estimation of the helical parameters of the NMR and hybrid atomic models was performed with HELFIT [29]. The electrostatic potential map of the needle filament was calculated with APBS 1.5 using the automatic focusing method to solve the linearized Poisson-Boltzmann equation at the temperature of 37 °C and ionic strength 150 mM with multiple Debye-Hückel spheres boundary conditions [30]. Respective images were produced with PyMOL 2.4.1 (Schrödinger, LLC). Plots were made with matplotlib [31]. Additional graphics were done with Inkscape (Inkscape contributors, https://inkscape.org).

## 3. Results and discussion

### 3.1. Start-end coordinates for attached type 3 filaments can be obtained from basal body coordinates

To date, all published high-resolution cryo-EM structures of type 3

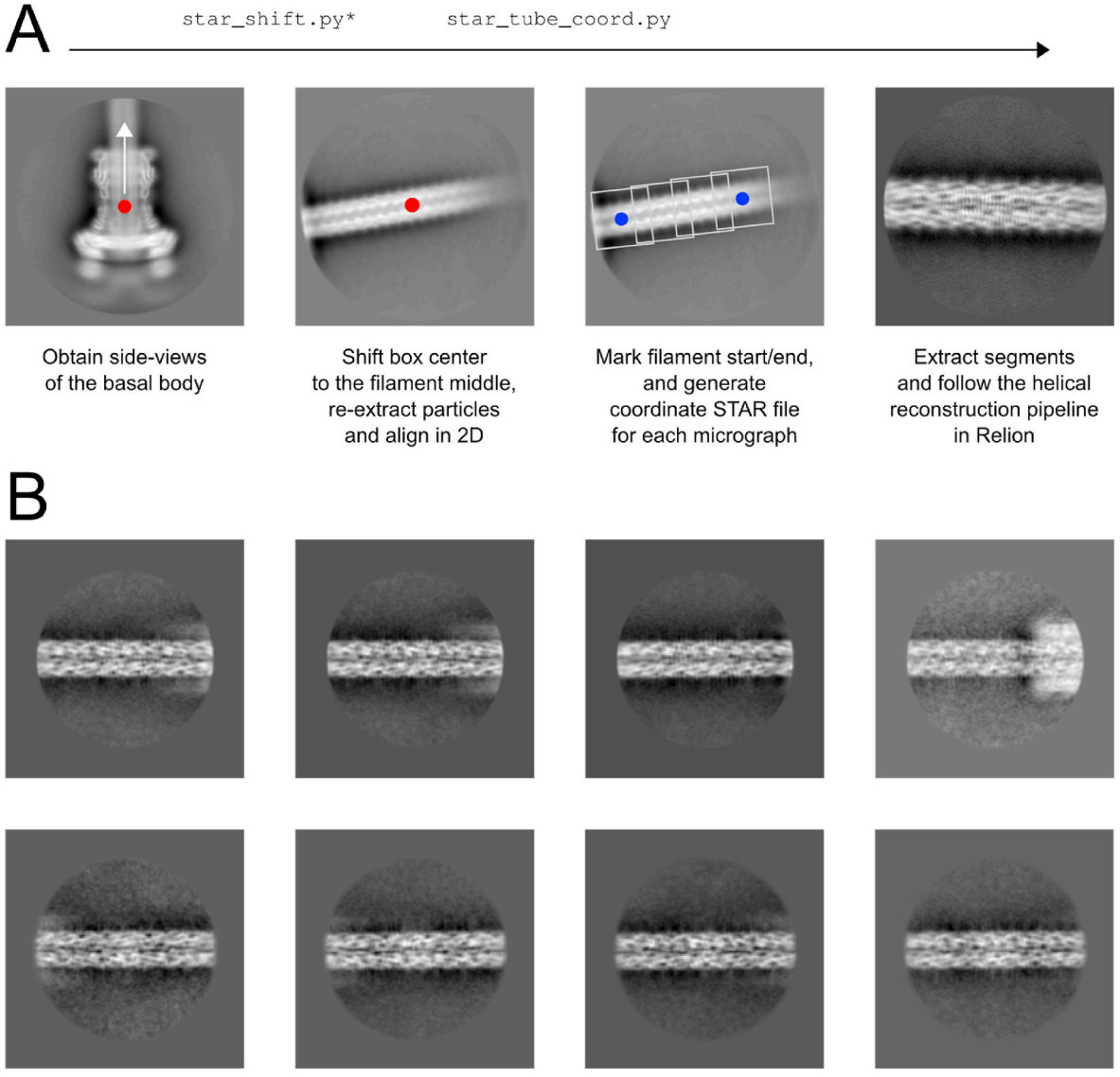


**Fig. 1. Workflow to obtain helical segments from type 3 needle filaments attached to the basal body**
A - Particles that are guaranteed to be basal bodies of the type 3 secretion system are obtained by conventional single particle reconstruction. The STAR file with particles representing side-views of the complex from a single class (*_data.star) is used to shift the box center (red dot) to the middle of the filament. This can be achieved with either star_shift.py script presented in this work or using "Recenter refined coordinates" option in Extract job of Relion 3. The filaments can be optionally re-aligned using 2D classification to account for the movement of the filament relative to the basal body. The coordinates of the start and end of the helix (blue dots, coordinate of the box center is (0, 0)) are supplied to star_tube_coord.py script, which generates a start/end coordinate STAR file for each micrograph. Once the coordinates are imported into Relion, they can be used to create segments for subsequent analysis with the standard helical reconstruction pipeline. All images in the panel are exemplary 2D class averages obtained from *Salmonella* data set and converted to PNG format using e2proc2d.py from EMAN2 suite [42].
B – Representative 2D class averages of segments obtained with the coordinate shift procedure (top row) or autopicking (bottom row). All images in the panel are from *Shigella* dataset. (For interpretation of the references to color in this figure legend, the reader is referred to the Web version of this article.)

needle filament relied on either manual picking [9,32] or autopicking [10] to produce segments for helical reconstruction. In cases where type 3 needle filaments are the only particles present in the sample (reconstituted needle filaments in Fujii et al., sheared-off needle filaments in Hu et al.) these approaches have no alternatives. However, when a fully assembled type 3 needle complex is present in the sample, it would be a great advantage to obtain needle filament start and end coordinates based on the offset from the basal body.

Type 3 needle complexes tend to adopt side-view orientation on the cryo-EM support, so the offsets can be calculated from 2D class averages (Fig. 1). The coordinates of basal body centers on the micrograph and their in-plane rotation angle ψ required to produce the class average are stored in Relion STAR file in fields rlnCoordinateX, rlnCoordinateY and rlnAnglePsi. The offsets from the basal body can be measured using Relion display utility, and then the particle box center can be shifted to the new position:

$$x' = x + \Delta x \Delta cos\psi + \Delta y \Delta sin\psi$$

$$y' = y - \Delta x \Delta sin\psi + \Delta y \Delta cos\psi$$

where x and y are basal body micrograph coordinates, Δx and Δy are offsets from the basal body, x′ and y′ are the new coordinates on the micrograph.

Depending on the strain and purification procedure, type 3 needle filaments reach lengths of 40 nm and more in purified needle complexes. Consequently, in basal body single particle reconstruction the needle filaments are usually cropped by the particle box. Thus, the box center must be first shifted from the basal body to the middle of the needle filament (Fig. 1) in order to bring the filament in the focus of the single particle reconstruction. Since the needle filament may move relative to the basal body (as demonstrated in Supplementary movie 1 from Ref. [33]), another particle alignment step should be performed after the box center shift. Finally, based on the 2D class average of the aligned needle filament the offsets from the box center corresponding to helix start and helix end can be calculated from rlnCoordinateX, rlnCoordinateY and rlnAnglePsi and stored in a coordinate STAR file for each micrograph. Python 3 scripts performing these manipulations and detailed instructions are available in the Supplemental data 1.

The proposed procedure has several advantages. First, the starting dataset of basal bodies usually contains high-quality particles, which were cleaned-up and validated in a separate 3D reconstruction (e.g. of the basal body inner or outer ring). Thus, high-quality segments can be obtained straight away without additional clean-up steps, which are usually required for autopicked particles. As demonstrated in Fig. 1B, the 2D class averages have very similar appearance of the picking procedure used, however, the coordinate shift procedure required less time and computational resources compared to autopicking, because the size of the starting dataset was much smaller. Second, the proposed procedure ensures that all filaments used in the single particle reconstruction are attached to the basal body. In contrast, helical autopicking on a basal body sample will not distinguish attached filaments and contamination with sheared-off filaments. Third, this procedure unambiguously assigns the polarity of the helix. In Relion helical reconstruction the orientation of the filament is used to calculate priors of the in-plane rotation angle ψ for the helical segments. While a proper initial estimate of helix orientation is not a critical parameter given the quality of modern cryo-EM datasets, a good estimate of this value can improve the

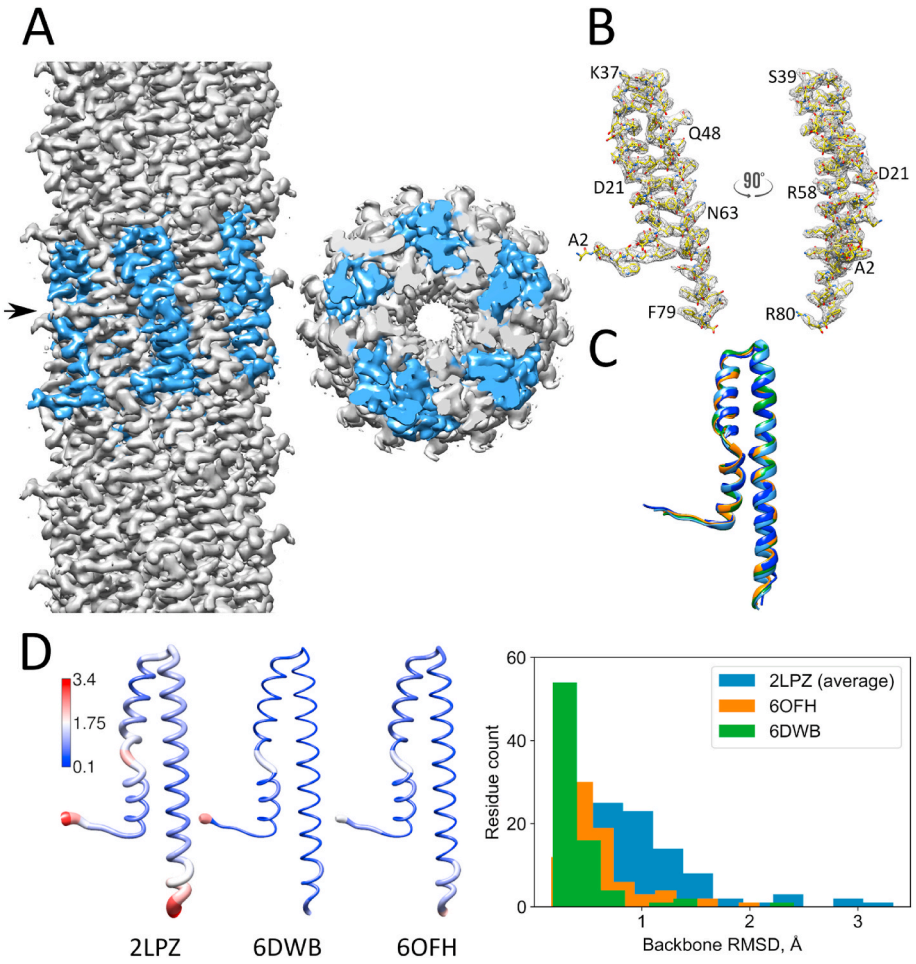


**Fig. 2. High-resolution structure of *Salmonella* needle filament attached to the basal body.**
A - Side view (left) and cross-section (right) of the map with six consecutive subunits of the 11-start helix (i.e. belonging to more than one turn) colored in light blue; arrow points to the location of the cross-section
B – Stick representation of PrgI protomer placed inside the cryo-EM map; individual residues are labeled to show the orientation of the polypeptide chain.
C - Superposition of our PrgI protomer model (light blue), with the model 1 of the solid-state NMR structure (dark blue, PDB code 2LPZ), the detached needle cryo-EM model (green, PDB code 6DWB) and the basal body-attached cryo-EM model (orange, PDB code 6OFH).
D - PrgI in worm representation and histogram distribution showing the per-residue backbone RMSD between our model and the protomer from other reconstructions: solid-state NMR model (PDB code 2LPZ, average RMSD of the ten models), detached filament cryo-EM model (PDB code 6DWB), attached filament cryo-EM model (PDB code 6OFH). The worm diameter is proportional to the RMSD. The color from blue to white to red also visualizes the increasing RMSD, color scale with values in Ångstrom is also shown. (For interpretation of the references to color in this figure legend, the reader is referred to the Web version of this article.)

efficiency of the 2D classification.

### 3.2. Helical structure of the Salmonella needle filament obtained with the new procedure agrees with the previously published results

In order to validate the procedure we performed 3D reconstruction of *Salmonella* type 3 needle filament attached to the basal body (Fig. 2A and B) reaching 3.6 Å gold-standard resolution (Supplemental Figure 1). Refined helical parameters (twist 63.36°, rise 4.4 Å) are close to the previously published structures (Supplemental Table 1). The overall conformation of the PrgI protomer is also consistent with published results (Fig. 2C): after superposition Cα RMSD with published cryo-EM structures [9,10] is 0.5–0.6 Å, while the average Cα RMSD with an NMR ensemble [7] is 1.1–1.2 Å between 67 superposed residues, increasing to 1.43 Å when all shared 79 residues are included. Overall, the distribution of per-residue Cα RMSD between our model and published structures is much wider in case of the NMR ensemble (see histogram in Fig. 2D). The highest local differences are observed in the flexible regions including N-terminus, kink and turn as well as in the C-terminal region (Fig. 2D, Supplemental Table 2). Thus, the proposed procedure yields a 3D structure of type 3 filament that is overall very similar to other approaches for cryo-EM data processing.

Our results corroborate that the conformation of the *Salmonella* type 3 needle filament that is exposed to the extracellular space does not depend on its attachment to the basal body. It cannot be excluded, however, that the differences in the conformations are too subtle to be determined with the current resolution of the map (3.6. Å). A conclusive answer to this question requires a further increase in resolution and the possibility to assess local differences in helical symmetry and individual protomer conformations.

### 3.3. High resolution structure of Shigella type 3 needle filament

We next applied the validated procedure to the type 3 needle filament of *Shigella*, for which no high-resolution cryo-EM structure is available yet. Therefore, we extracted the needle filaments from a dataset used previously for the reconstruction of the *Shigella* needle complex [17]. Using the described procedure we obtained a map with 3.6 Å gold-standard resolution (Fig. 3A and B, Supplemental Figure 1). Comparing both filament structures, we found that helical arrangement of the MxiH protomer is very similar to the helix determined for *Salmonella*, and to a model determined by a hybrid approach combining solid-state NMR and cryo-EM (Fig. 3C) [8]. However, in contrast to the map used for the previously published hybrid reconstruction, the resolution of our map allows for the first time the unambiguous tracing of backbone and side chains for most of the residues. The MxiH protomer adopts the helix-turn-helix topology, with a kink in the middle of the N-terminal helix (residues T23-Q24), a loop at the N-terminus including the first 11 residues and a tight C-terminal turn with helical $3_{10}$ conformation (residues I79–F82) (Fig. 3B). Consistently with the previously determined type 3 needle structures, the helical filament defines an inner channel with about 20 Å diameter and has an outer diameter of approximately 70 Å.

Similarly to the *Salmonella* needle, the helical arrangement of the

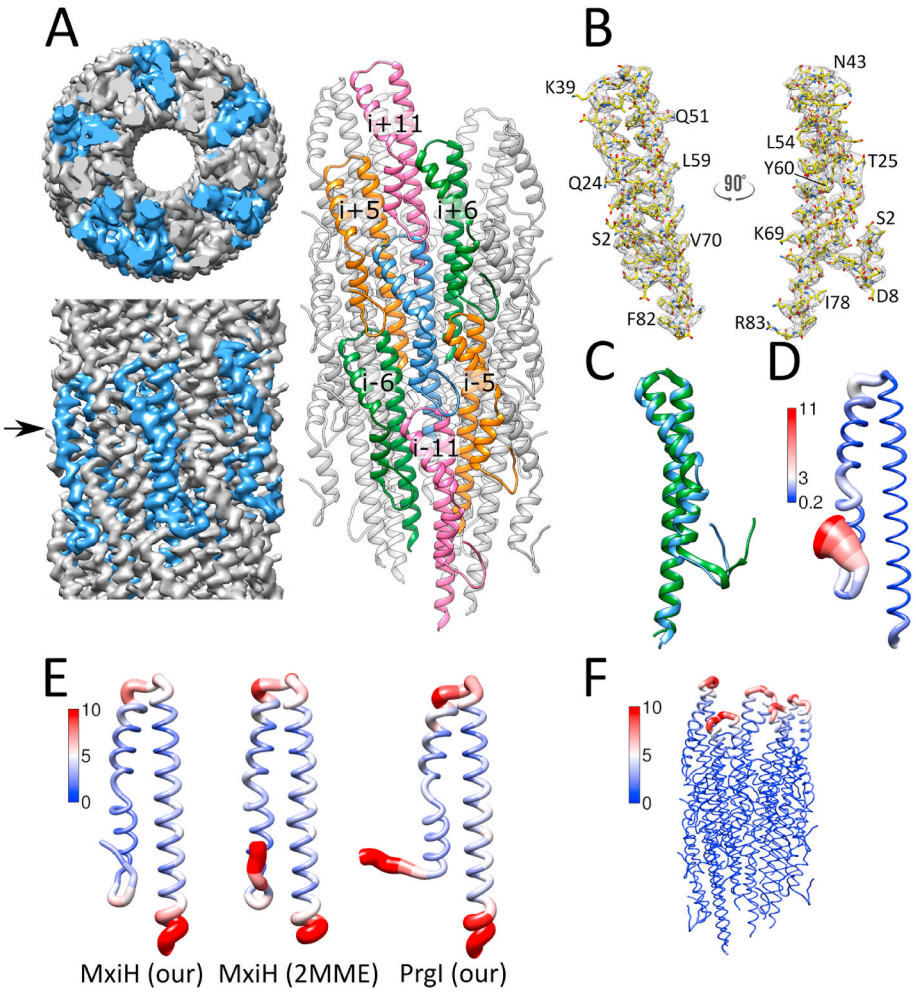


**Fig. 3. High-resolution structure of the *Shigella* needle filament attached to the basal body.** A - Side view (lower left) and cross-section (upper left) of the map with six consecutive subunits of the 11-start helix (i.e. belonging to more than one turn) colored in light blue; arrow points to the location of the cross-section. In the needle cartoon model (right), the blue subunit forms the i±5 interfaces with the orange subunits, the i±6 interfaces with the green subunits and the i±11 interfaces with the pink subunits. B - Stick representation of MxiH protomer placed inside the cryo-EM map; individual residues are labeled to show the orientation of the polypeptide chain. C - Superposition between our MxiH model (blue) and the hybrid model (PDB code 2MME, model 1, green) showing the different conformation of the N-terminal loop. D - MxiH in worm representation depicting per-residue backbone RMSD between our model and the protomer from the hybrid reconstruction (PDB code 2MME, average RMSD of the ten models). The worm diameter is proportional to the RMSD. The color from blue to white to red also visualizes the increasing RMSD, the scale with values in Ångstrom is also shown. E – Fluctuations from NMA in worm representation of our MxiH model, the MxiH hybrid reconstruction (PDB code 2MME) and our PrgI model. The worm diameter is proportional to the per-residue fluctuations in the range 0–10 Å. The color from blue to white to red also visualizes the increasing fluctuations in the same range, color scale is shown with values in Å. F- Fluctuations from NMA in worm representation of the distal end of the MxiH needle filament. The worm diameter and the color scale visualize the fluctuations in the 0–10 Å range. NMA of the filament model shows fluctuation also at the termini of the subunits of the proximal end, which has been hidden as artifactual, since these subunits do not form a free end but are bound to the inner rod or export apparatus. (For interpretation of the references to color in this figure legend, the reader is referred to the Web version of this article.)

subunits resembles the architecture of the flagellar filament [7,34]. Each MxiH protomer forms extensive contacts with six others, defining three interfaces (Fig. 3A). The most extended interface (~840 Å$^2$, 13% of the protomer surface) is formed by contacts with the i±5 subunits. The second half of the N-terminal helix is in contact with the helical kink and the N-terminal loop of the neighbor, while residues of the turn and of the C-terminal helix contact residues of the C-terminal helix in the nearby protomer. The second interface (~630 Å$^2$, 10% of the protomer surface) arises from the adjacent i±6 subunits and involves the beginning of the N-terminal helix of one subunit and C-terminal helix of both subunits. The smallest interface (~500 Å$^2$, 8% of the protomer surface) is created by end-to-end contacts with the almost stacked i±11 subunits, where residues of the turn or close to the turn of one molecule interact with the terminal residues of the other.

The positively charged side chains of residues K69, K72 and R83, partially neutralized by the negatively charged C-terminus and D73, define a right-handed spiral on the surface of the needle lumen (Supplemental Figure 2A), similarly to the *Salmonella* needle [10]. However, the negatively charged residues are the majority in MxiH (net charge −4), and the electrostatic potential results negative on the outer and inner surface of the hollow needle (Supplemental Figure 2B), in contrast to what has been observed in the PrgI needle where positively charged spots appear on the lumen surface [9].

### 3.4. Comparison with the hybrid model of Shigella type 3 needle filament

The overall arrangement of the helical needle structure determined in this study agrees well with the model previously determined by solid state NMR and cryo-EM [8]. The helical rise and the twist of our model are 64.05° and 4.31 Å, respectively (Table 1, Supplemental Table 1), consistent with the parameters of the hybrid model, determined from the ten models of the ensemble deposited at the wwPDB with code 2MME, which are 64.10 ± 0.06° and 4.33 ± 0.02 Å. Similarly, the low-resolution cryo-EM map used to refine the hybrid models [32] has a twist of 64.06° and a rise of 4.30 Å. Thus, we do not find significant differences in the helical architecture from reconstructions obtained by different experimental techniques or different assembly mechanism of the needle. This is in contrast to what is reported by Guo et al. [9], where the differences in the helical parameters of the reconstruction of the *Salmonella* needle are ascribed to the different experimental approaches, i.e. cryo-EM versus solid state NMR. We suppose, however, that inclusion of a low-resolution cryo-EM map as an additional constraint for the *Shigella* hybrid model is probably responsible for the good agreement of the parameters with our reconstruction.

Overall, the MxiH protomer topology derived by the hybrid reconstruction is consistent with our model, and there is good agreement in the helical regions of the structures. The average Cα RMSD between the ten hybrid models and our structure is 0.94 Å for 67 superposed residues and it increases to 2.25 Å including all the 82 residues. Analysis of the average per-residue backbone RMSD (Fig. 3D, Supplemental Table 2) and visual inspection shows a different conformation of the N-terminal loop in the two structures (Supplemental Figure 3A). Of note, the hybrid model does not describe well the corresponding density from the low-resolution cryo-EM map (Supplemental Figure 3B). The observed differences in conformation might be responsible for the strong increase of the Cα RMSD when calculated including all the residues, but also smaller deviations at the turn and at the kink, likely due to their greater flexibility, and at the C-terminus, where the last $3_{10}$-helical turn of our reconstruction fits the EM density better than the α-helix of the hybrid models. The more ordered and stiff α-helices in the rest of the structure show the strongest agreement between our reconstruction and the hybrid models.

The N-terminal loop forms a helical turn in the hybrid models and then it extends on the outer surface of the needle filament subunit i-5, while in our reconstruction the loop is sandwiched between different chains and folds back toward the first half of the N-terminal helix of the same subunit (Fig. 3C). As a consequence, the i±5 interface is bigger in hybrid models (~950 Å$^2$) and the *i±6* interface is smaller (~480 Å$^2$).

The stretch comprising residues M1 to V5 is dispensable and can be deleted from the needle protomer without affecting the functionality of the type 3 secretion system [4]. However, P6 and downstream residues are essential for a functional needle [35]. For these reasons, it is interesting to speculate whether the observed conformation of the N-terminal loop has any implications for the needle filament organization. Normal mode analysis (NMA) is an established computational method to predict functionally-relevant motions available to a protein molecule [36]. We used the NMA pipeline from R package bio3D [23,24] to assess the possible motions in the MxiH protomer (Fig. 3E). In the hybrid models the N-terminus of the protomer is highly fluctuating, and this behavior is similar to *Salmonella* PrgI. In contrast, in our MxiH model the magnitude of fluctuations predicted by NMA is lower. Of note, our preparation of MxiH contains a presumably disordered N-terminal Strep-tag, while the hybrid models were built from a sample without additional tags. Disordered tags can decrease the stability of the protein, however, in our model we observe fewer fluctuations in NMA as compared to a tag-free structure. This suggests that the N-terminal loop region may contribute to the overall stability and packing of the *Shigella* filament.

Interestingly, NMA of the MxiH needle model including 23 protomers, shows stabilization of the protomer termini, while fluctuations occur in the turn region of the five subunits at the distal end (Fig. 3F). The flexibility of this region might allow binding of additional subunits to extend the growing needle.

The N-terminus also binds the turn of the i-11 subunit, forming the so-called protofilaments in the Calladine's model of the flagellar filament [37], thus causing a conformational difference also in that region. Mutation of W10 or L12, residues where the N-terminal loop becomes helix and which are involved in the i-11 interaction with the turn of the neighbors, have been shown to have dramatic effects on the filament length or on the ability of *Shigella* to invade host cells [35]. Similarly, mutations of the turn residues subvert the controlled secretion of effectors, impairing the ability of the bacteria to invade host cells.

The turn region is also in contact with the kink of the neighboring *i*+5 subunit. Although not conclusively defined by the density map, T23, the residue at the center of the kink, seems to form a hydrogen bond with the turn of the neighboring subunit (Fig. 4). Interestingly, this bond is not present in the hybrid models, because of the different rotamer adopted by T23, which appears to be coupled to the rotameric conformation of Y60, in our reconstruction also diverging from the hybrid models (but fully supported by the density map in our model). Y60 is in the middle of the C-terminal helix, which defines the channel's inner surface, thus it is tempting to speculate that it could trigger and propagate a conformational change of the needle structure, or a signal, by acting on the flexible kink and turn regions.

Among the most critical residues found by alanine scanning and deletion mutagenesis [35], the very C-terminal residues are essential for the needle complex formation. Besides lining the inner surface of the channel, these residues are also involved in all the three interfaces of the helical filament. Similarly to Y60, F82 adopts different rotamers in our reconstruction and in the hybrid models (Fig. 4), and its conformation appears to be sterically coupled to Q51 of the i-11 subunit, which is immediately below on the "protofilament" stack. The side chains of Q51 and F82 point in almost opposite directions, and they are swapped in our reconstruction compared to the hybrid models, suggesting that both are stable conformations. It is tempting to speculate that the two conformations are the two states of a switch. Very interestingly, the mutation Q51A has been found to produce constitutive secretion, causing an unregulated release of translocons and early effectors [35], and to affect signal transduction from the needle tip [38].

## 4. Conclusion

In this work we presented an easy-to-use approach for helical

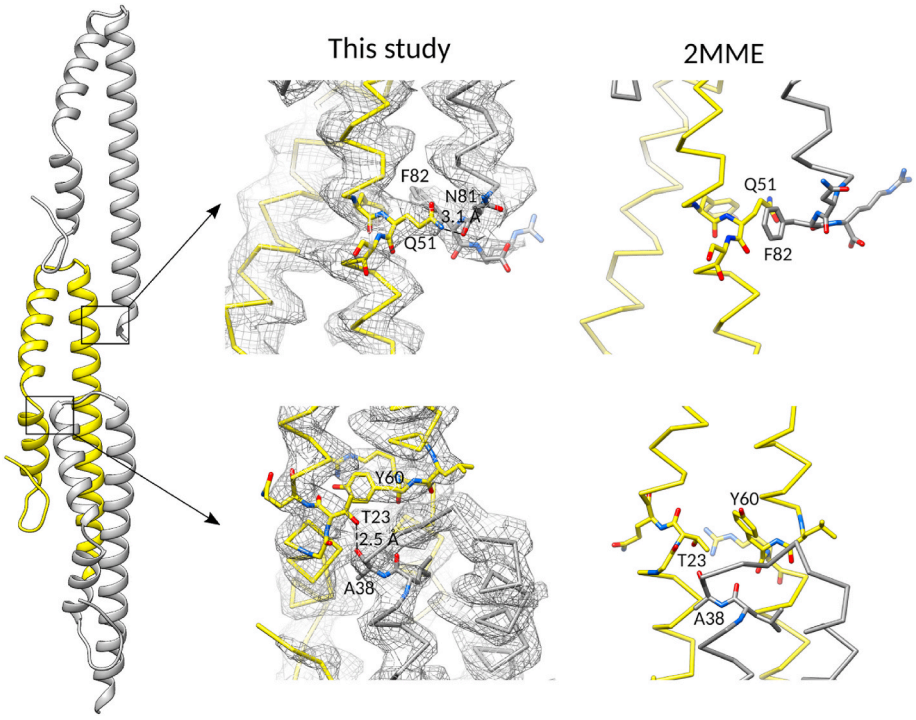


**Fig. 4. Close-up of residues adopting different conformation in our MxiH model and in the hybrid reconstruction.** Stick models of the different conformations of the head-tail residues of the stacked subunits (top) and of the kink residues (bottom) between our MxiH model (left, also with the density map) and the model 1 of the hybrid reconstruction (right, PDB code 2MME). The orientation of the molecules is similar for the two models. Different subunits have different color of the carbon atoms. The overview of the three subunits forming the two interfaces is shown on the left. The residues 22–24, 50–52 and 59–61 (yellow subunit), 37–38 and 81–83 (gray subunits) are represented as stick; other residues are represented as Cα trace for clarity. (For interpretation of the references to color in this figure legend, the reader is referred to the Web version of this article.)

reconstruction of type 3 needle filaments attached to the basal body. The procedure can be readily applied to existing datasets, and potential applications are not limited to pathogenic type 3 secretion systems. We believe it is applicable to all cases where side-views of a relatively straight helical structure attached to another structure are available. Examples of such assemblies include pili (type IV secretion systems) [39] and tailed phages [40,41].

When applied to the well-studied example of *Salmonella* PrgI needle filaments, the procedure yields a model that is highly consistent with previously published data. Importantly, the laborious steps of manual picking or helical autopicking followed by removal of low-quality particles are omitted during single particle processing. We next applied our procedure to a recently published dataset of *Shigella* type 3 secretion systems to yield the highest resolution structure to date of attached MxiH needle filament. Compared to the previously solved structure of *in vitro* reconstituted MxiH needle filament, our model contains a different conformation of the N-terminal loop and shows different rotameric conformation in several potentially critical residues in the kink region and C-terminal helix of the protomer.

## Declaration of competing interest

The authors declare that they have no known competing financial interests or personal relationships that could have appeared to influence the work reported in this paper.

## Acknowledgements

This work was funded by the European Research Council under the European Community's Seventh Framework Programme (https://erc.europa.eu/) under grant number 311374. This work has been supported by iNEXT, grant number 653706, funded by the Horizon 2020 programme of the European Commission.

This project was supported by funds available to TCM at the Institute of Structural and Systems Biology at the University Medical Center Hamburg-Eppendorf.

Part of this work was performed at the EM facility at CSSB, supported by UHH and DFG grant numbers (INST 152/772–1|152/774–1|152/775–1|152/776–1|152-777-1 FUGG). The Core Facility Cryo-electron Microscopy and Tomography of CEITEC Masaryk University is gratefully acknowledged for the obtaining of the scientific data used for the MxiH reconstruction. We thank Jiří Nováček and Antje Kamprad for helping in the MxiH sample delivery and data collection. This research was supported through the Maxwell computational resources operated at Deutsches Elektronen-Synchrotron (DESY), Hamburg, Germany.

## Appendix A. Supplementary data

Supplementary data to this article can be found online at https://doi.org/10.1016/j.bbrep.2021.101039.

## Author contributions

Conceptualization: VK, MK, TCM.
Methodology: VK, ML, JW.
Software: VK.
Investigation: VK, ML, JW.
Formal Analysis: VK, ML.
Visualization: ML, VK.
Data Curation: ML, VK.
Resources: ML, JW, TCM.
Writing –Original Draft: ML, VK.
Writing –Review & Editing: ML, VK, JW, MK, TCM.
Supervision: MK, TCM.
Funding Acquisition: ML, MK, TCM.

## References

[1] J.E. Galan, M. Lara-Tejero, T.C. Marlovits, S. Wagner, Bacterial type III secretion systems: specialized nanomachines for protein delivery into target cells, Annu. Rev. Microbiol. 68 (2014) 415–438, https://doi.org/10.1146/annurev-micro-092412-155725.

[2] S. Dey, A. Chakravarty, P.G. Biswas, R.N.D. Guzman, The type III secretion system needle, tip, and translocon, Protein Sci. 28 (9) (2019) 1582–1593, https://doi.org/10.1002/pro.3682.

[3] L. Senerovic, S.P. Tsunoda, C. Goosmann, et al., Spontaneous formation of IpaB ion channels in host cell membranes reveals how Shigella induces pyroptosis in

macrophages, Cell Death Dis. 3 (9) (2012), https://doi.org/10.1038/cddis.2012.124 e384-e384.
[4] Poyraz Ö, H. Schmidt, K. Seidel, et al., Protein refolding is required for assembly of the type three secretion needle, Nat. Struct. Mol. Biol. 17 (7) (2010) 788–792, https://doi.org/10.1038/nsmb.1822.
[5] Y. Wang, A.N. Ouellette, C.W. Egan, T. Rathinavelan, W. Im, R.N. De Guzman, Differences in the electrostatic surfaces of the type III secretion needle proteins PrgI, BsaL, and MxiH, J. Mol. Biol. 371 (5) (2007) 1304–1314, https://doi.org/10.1016/j.jmb.2007.06.034.
[6] V.E. Galkin, W.H. Schmied, O. Schraidt, T.C. Marlovits, E.H. Egelman, The structure of the Salmonella typhimurium type III secretion system needle shows divergence from the flagellar system, J. Mol. Biol. 396 (5) (2010) 1392–1397, https://doi.org/10.1016/j.jmb.2010.01.001.
[7] A. Loquet, N.G. Sgourakis, R. Gupta, et al., Atomic model of the type III secretion system needle, Nature 486 (7402) (2012) 276–279, https://doi.org/10.1038/nature11079.
[8] J.-P. Demers, B. Habenstein, A. Loquet, et al., High-resolution structure of the *Shigella* type-III secretion needle by solid-state NMR and cryo-electron microscopy, Nat. Commun. 5 (2014) 4976, https://doi.org/10.1038/ncomms5976.
[9] E.Z. Guo, D.C. Desrosiers, J. Zalesak, et al., A polymorphic helix of a Salmonella needle protein relays signals defining distinct steps in type III secretion, PLoS Biol. 17 (7) (2019), e3000351, https://doi.org/10.1371/journal.pbio.3000351.
[10] J. Hu, L.J. Worrall, C. Hong, et al., Cryo-EM analysis of the T3S injectisome reveals the structure of the needle and open secretin, Nat. Commun. 9 (1) (2018) 3840, https://doi.org/10.1038/s41467-018-06298-8.
[11] S. He, S.H.W. Scheres, Helical reconstruction in RELION, J. Struct. Biol. 198 (3) (2017) 163–176, https://doi.org/10.1016/j.jsb.2017.02.003.
[12] S.T. Huber, T. Kuhm, C. Sachse, Automated tracing of helical assemblies from electron cryo-micrographs, J. Struct. Biol. 202 (1) (2018) 1–12, https://doi.org/10.1016/j.jsb.2017.11.013.
[13] T. Wagner, S. Raunser, The evolution of SPHIRE-crYOLO particle picking and its application in automated cryo-EM processing workflows, Commun Biol 3 (1) (2020) 1–5, https://doi.org/10.1038/s42003-020-0790-y.
[14] Y. Zhu, B. Carragher, D.J. Kriegman, R.A. Milligan, C.S. Potter, Automated identification of filaments in cryoelectron microscopy images, J. Struct. Biol. 135 (3) (2001) 302–312, https://doi.org/10.1006/jsbi.2001.4415.
[15] O. Schraidt, M.D. Lefebre, M.J. Brunner, et al., Topology and organization of the Salmonella typhimurium type III secretion needle complex components, PLoS Pathog. 6 (4) (2010), e1000824, https://doi.org/10.1371/journal.ppat.1000824.
[16] N. Goessweiner-Mohr, V. Kotov, M.J. Brunner, et al., Structural control for the coordinated assembly into functional pathogenic type-3 secretion systems, bioRxiv (2019) 714097, https://doi.org/10.1101/714097. Published online July 24.
[17] M. Lunelli, A. Kamprad, J. Bürger, T. Mielke, C.M.T. Spahn, M. Kolbe, Cryo-EM structure of the Shigella type III needle complex, PLoS Pathog. 16 (2) (2020), e1008263, https://doi.org/10.1371/journal.ppat.1008263.
[18] J. Zivanov, T. Nakane, B.O. Forsberg, et al., New tools for automated high-resolution cryo-EM structure determination in RELION-3. Egelman EH, Kuriyan J, eLife 7 (2018), e42166, https://doi.org/10.7554/eLife.42166.
[19] E.F. Pettersen, T.D. Goddard, C.C. Huang, et al., UCSF Chimera—a visualization system for exploratory research and analysis, J. Comput. Chem. 25 (13) (2004) 1605–1612, https://doi.org/10.1002/jcc.20084.
[20] T.D. Goddard, C.C. Huang, E.C. Meng, et al., UCSF ChimeraX: meeting modern challenges in visualization and analysis, Protein Sci Publ Protein Soc 27 (1) (2018) 14–25, https://doi.org/10.1002/pro.3235.
[21] P. Emsley, B. Lohkamp, W.G. Scott, K. Cowtan, Features and development of Coot, Acta Crystallogr D Biol Crystallogr 66 (4) (2010) 486–501, https://doi.org/10.1107/S0907444910007493.
[22] D. Liebschner, P.V. Afonine, M.L. Baker, et al., Macromolecular structure determination using X-rays, neutrons and electrons: recent developments in Phenix, Acta Crystallogr Sect Struct Biol 75 (10) (2019) 861–877, https://doi.org/10.1107/S2059798319011471.
[23] B.J. Grant, A.P.C. Rodrigues, K.M. ElSawy, J.A. McCammon, L.S.D. Caves, Bio3d: an R package for the comparative analysis of protein structures, Bioinformatics 22 (21) (2006) 2695–2696, https://doi.org/10.1093/bioinformatics/btl461.
[24] L. Skjærven, X.-Q. Yao, G. Scarabelli, B.J. Grant, Integrating protein structural dynamics and evolutionary analysis with Bio3D, BMC Bioinf. 15 (1) (2014) 399, https://doi.org/10.1186/s12859-014-0399-6.
[25] W. McKinney, Data structures for statistical computing in Python, in: S. van der Walt, J. Millman (Eds.), Proceedings of the 9th Python in Science Conference, 2010, pp. 51–56.
[26] T.E. Oliphant, Guide to NumPy, second ed., CreateSpace Independent Publishing Platform, 2015.
[27] E.C. Meng, E.F. Pettersen, G.S. Couch, C.C. Huang, T.E. Ferrin, Tools for integrated sequence-structure analysis with UCSF Chimera, BMC Bioinf. 7 (1) (2006) 339, https://doi.org/10.1186/1471-2105-7-339.
[28] E. Krissinel, K. Henrick, Inference of macromolecular assemblies from crystalline state, J. Mol. Biol. 372 (3) (2007) 774–797, https://doi.org/10.1016/j.jmb.2007.05.022.
[29] P. Enkhbayar, S. Damdinsuren, M. Osaki, N. Matsushima, HELFIT: helix fitting by a total least squares method, Comput. Biol. Chem. 32 (4) (2008) 307–310, https://doi.org/10.1016/j.compbiolchem.2008.03.012.
[30] N.A. Baker, D. Sept, S. Joseph, M.J. Holst, J.A. McCammon, Electrostatics of nanosystems: application to microtubules and the ribosome, Proc. Natl. Acad. Sci. U. S. A. 98 (18) (2001) 10037–10041, https://doi.org/10.1073/pnas.181342398.
[31] J.D. Hunter, Matplotlib: a 2D graphics environment, Comput. Sci. Eng. 9 (3) (2007) 90–95, https://doi.org/10.1109/MCSE.2007.55.
[32] T. Fujii, M. Cheung, A. Blanco, T. Kato, A.J. Blocker, K. Namba, Structure of a type III secretion needle at 7-Å resolution provides insights into its assembly and signaling mechanisms, Proc. Natl. Acad. Sci. Unit. States Am. 109 (12) (2012) 4461–4466, https://doi.org/10.1073/pnas.1116126109.
[33] O. Schraidt, T.C. Marlovits, Three-dimensional model of Salmonella's needle complex at subnanometer resolution, Science 331 (6021) (2011) 1192–1195, https://doi.org/10.1126/science.1199358.
[34] C.R. Calladine, B.F. Luisi, J.V. Pratap, A "mechanistic" explanation of the multiple helical forms adopted by bacterial flagellar filaments, J. Mol. Biol. 425 (5) (2013) 914–928, https://doi.org/10.1016/j.jmb.2012.12.007.
[35] R. Kenjale, J. Wilson, S.F. Zenk, et al., The needle component of the type III secreton of Shigella regulates the activity of the secretion apparatus, J. Biol. Chem. 280 (52) (2005) 42929–42937, https://doi.org/10.1074/jbc.M508377200.
[36] I. Bahar, T.R. Lezon, A. Bakan, I.H. Shrivastava, Normal mode analysis of biomolecular structures: functional mechanisms of membrane proteins, Chem. Rev. 110 (3) (2010) 1463–1497, https://doi.org/10.1021/cr900095e.
[37] C. Wang, M. Lunelli, E. Zschieschang, J.B. Bosse, R. Thuenauer, M. Kolbe, Role of flagellar hydrogen bonding in Salmonella motility and flagellar polymorphic transition, Mol. Microbiol. 112 (5) (2019) 1519–1530, https://doi.org/10.1111/mmi.14377.
[38] I. Murillo, I. Martinez-Argudo, A.J. Blocker, Genetic dissection of the signaling cascade that controls activation of the Shigella type III secretion system from the needle tip, Sci. Rep. 6 (1) (2016) 27649, https://doi.org/10.1038/srep27649.
[39] R. Fronzes, P.J. Christie, G. Waksman, The structural biology of type IV secretion systems, Nat. Rev. Microbiol. 7 (10) (2009), https://doi.org/10.1038/nrmicro2218.
[40] L.A. Amos, A. Klug, Three-dimensional image reconstructions of the contractile tail of T4 bacteriophage, J. Mol. Biol. 99 (1) (1975) 51–64.
[41] P.G. Leiman, P.R. Chipman, V.A. Kostyuchenko, V.V. Mesyanzhinov, M. G. Rossmann, Three-Dimensional rearrangement of proteins in the tail of bacteriophage T4 on infection of its host, Cell 118 (4) (2004) 419–429, https://doi.org/10.1016/j.cell.2004.07.022.
[42] G. Tang, L. Peng, P.R. Baldwin, et al., EMAN2: an extensible image processing suite for electron microscopy, J. Struct. Biol. 157 (1) (2007) 38–46, https://doi.org/10.1016/j.jsb.2006.05.009.